A New Family of Nonredundant Transforms Using Hybrid Wavelets and Directional Filter Banks

Ramin Eslami, *Member, IEEE*, and Hayder Radha, *Senior Member, IEEE*

***Abstract*—We propose a new family of nonredundant geometrical image transforms that are based on wavelets and directional filter banks. We convert the wavelet basis functions in the finest scales to a flexible and rich set of directional basis elements by employing directional filter banks, where we form a nonredundant transform family, which exhibits both *directional* and *nondirectional* basis functions. We demonstrate the potential of the proposed transforms using nonlinear approximation. In addition, we employ the proposed family in two key image processing applications, image coding and denoising, and show its efficiency for these applications.**

***Index Terms*—Directional filter banks (DFBs), geometrical image transforms, image coding, image denoising, nonlinear approximation (NLA), wavelet transform (WT).**

I. Introduction

RECENTLY, there have been several studies showing that separable 2-D wavelets fail to represent images optimally [28], [40]. It is well known that the wavelet transform provides efficient approximation of 1-D piecewise smooth signals; nevertheless, since natural images possess 1-D singularities in the form of regular edges, approximation behavior of 2-D wavelets for images indicates the need for further improvement [8], [40]. As a means to offset this deficiency to some extent, most image processing systems utilizing the wavelet transform, for instance coding and denoising systems, usually take advantage of a post-processing stage to treat the inter- and intrascale dependencies amongst the wavelet coefficients [34]–[36]. However, this approach alone does not necessarily eliminate the demand and need for more efficient image transforms.

To construct an efficient image transform, the following criteria are critical. First, the transform should provide a good *nonlinear approximation* (NLA) [28] behavior. This requires the transform to be direction sensitive (or geometric) in addition to being able to provide perfect reconstruction, multiresolution representation, and localized analysis. Other important features include the transform performance in terms of introducing a minimum level of ringing artifacts during NLA. The second criterion is that the transform should incur reasonable computational complexity. In the light of this property, fixed-procedure transforms are more desirable in contrast to the adaptive transforms, which normally impose more computations. Finally, being nonredundant is a requirement in some image processing tasks, most notably image coding.

In this paper, we introduce a new family of image transforms fulfilling the aforementioned criteria, study their properties and show their applications to coding and denoising of natural images. This family is one of the first nonadaptive directional approaches that is employed for image coding. The proposed transform family is constructed using *hybrid wavelets and directional filter banks* (HWD); thus, we refer to them as the HWD transforms.

Other nonredundant geometrical image transforms include bandelets [26], CRISP-contourlets [27], directionlets [39], nonredundant complex wavelets [22], and multiresolution direction filter banks [29]. A primary difference between our proposed transform family and the other nonredundant transforms mentioned above is the following. While HWD is nonadaptive, it possesses a rich set of directions, and provides an efficient NLA by taking advantage of the wavelet transform in its construction, and, thus, it could be directly employed in key image processing applications such as coding. We should also note that there have been a few attempts in the past to increase the directionality of wavelets using checkerboard filter bank [3], [10]. Although these transforms provide nonadaptive directional extension of wavelets, they are limited to a small number of directions and do not have flexibility when compared with our proposed scheme.

The paper is organized as follows. In the next section, we briefly present background material and the notations required for developing the proposed scheme. In Section III, we explain the construction of the proposed HWD transform family. In Section IV, we provide multiresolution analysis and efficient realization of the transforms. The applications of the proposed family as well as the experimental results are given in Section V, followed by our main conclusions in Section VI.

II. Background

A. Motivation

It is known that the *wavelet transform* (WT) fails to provide optimal NLA decay for images containing regular regions of $\boldsymbol{C}^{\alpha}(\alpha > 1)$ (i.e., α-order continuously differentiable regions)

Manuscript received January 24, 2006; revised October 11, 2006. This work was supported in part by the National Science Foundation under Award CCF-0515253, in part by MEDC Grant GR-296, in part by the Michigan State Foundation Intramural Research Grants Program, and in part by an unrestricted gift from Microsoft Research. The associate editor coordinating the review of this manuscript and approving it for publication was Prof. Ljubisa Stankovic.

R. Eslami was with the Department of Electrical and Computer Engineering, Michigan State University, East Lansing, MI 48824 USA. He is now with the Department of Electrical and Computer Engineering, McMaster University, Hamilton, ON L8S 4K1 Canada (e-mail: reslami@ieee.org).

H. Radha is with the Department of Electrical and Computer Engineering, Michigan State University, East Lansing, MI 48824 USA (e-mail: radha@egr.msu.edu).

Color versions of one or more of the figures in this paper are available online at http://ieeexplore.ieee.org.

Digital Object Identifier 10.1109/TIP.2007.891791

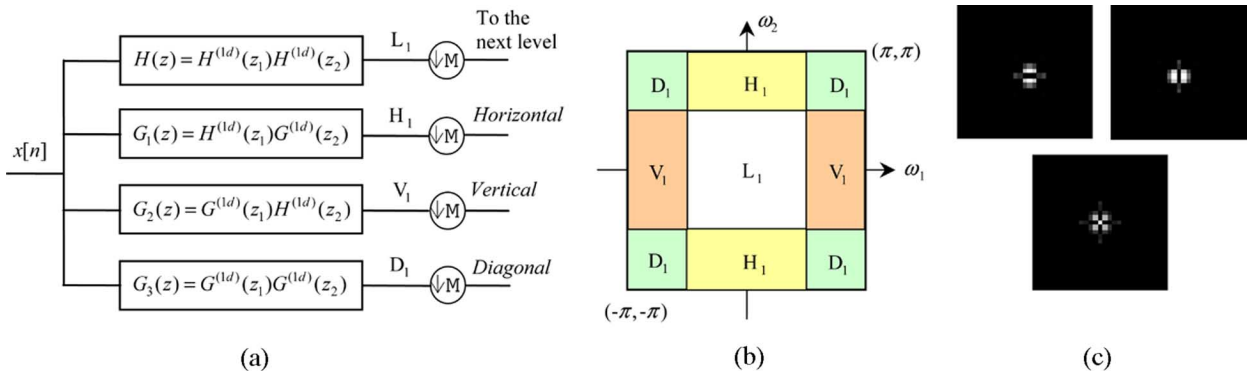

Fig. 1. (a) Two-dimensional separable wavelet transform. (b) The frequency partitioning of the separable wavelets. (c) Some basis functions corresponding to *Horizontal*, *Vertical*, and *Diagonal* subbands of biorthogonal 9/7 wavelets (from left to right). Note that only positive values are shown.

separated by regular discontinuities (or edges) of $\boldsymbol{C}^{\alpha}$. While the optimal decay rate of NLA is of $O(M^{-\alpha})$ where M is the number of retained coefficients during NLA, wavelets provide a decay rate of $O(M^{-1})$ [26], [28]. This low decay rate is due to the fact that the discontinuities in images yield many wavelet coefficients of large magnitude. That is, the regularity over the edges remains unseen from the WT. It turns out that there is quite ample room to further improve the NLA decay rate of wavelets.

In this paper, we attempt to pass wavelet coefficients through a filter bank in order to combine the large wavelet coefficients around discontinuities to achieve a more sparse representation. Although it is possible to construct a totally different basis from wavelets, we believe that improving wavelet basis has some key advantages.

- The discrete wavelet transform can be realized using a critically sampled filter bank and, consequently, provides a nonredundant image decomposition.
- Wavelets are popular in the image processing community and there exists numerous algorithms and procedures utilizing wavelets for image processing applications; hence, one can benefit from these algorithms by cleverly adapting them to the proposed transform family.
- Wavelet packets is an alternative to handle the problem adaptively. One can also enjoy this feature of wavelets when extending it for the proposed transforms.

Other leading approaches such as curvelets [8], [9] and contourlets [15] use a similar idea of combining large transform coefficients around discontinuities. The curvelet transform has been proposed in the continuous domain, and, therefore, implementing it in the discrete domain is challenging. The contourlet transform employs a Laplacian pyramid [6] to extract edges of an image and applies *directional filter banks* (DFB) [4] to all bandpass outputs of the pyramid with decreasing number of directions when moving to the coarser pyramid subbands. The DFB stage attempts to decorrelate the dependencies found over the edges in the bandpass outputs of the pyramid. The reason for choosing the Laplacian pyramid as the first stage is that because its highpass channels are not subject to downsampling, and, thus, there is no *frequency scrambling* for these channels. This construction, however, leads to the existing redundancy of the contourlet scheme, which makes this transform unsuitable for image coding.

Below we outline the notations we use in the paper. Then we very briefly present key aspects of the 2-D wavelet transform and DFB, which are required for the realization of the HWD family.

Notation: We denote a discrete d-dimensional signal by $x[\mathbf{n}]$ where $\mathbf{n} = (n_1, n_2, \ldots, n_d)$, and its z-transform as $X(\mathbf{z}) = \sum_{\mathbf{n}\in\mathbb{Z}^d} x[\mathbf{n}]\mathbf{z}^{-\mathbf{n}}$, where $\mathbf{z} = (z_1, z_2, \ldots, z_d)$ is a complex vector and $\mathbf{z}^{\mathbf{n}} = \prod_{i=1}^{d} z_i^{n_i}$. We also define $\mathbf{z}^M$ as $\mathbf{z}^M = (z^{m_1}, z^{m_2}, \ldots, z^{m_d})$, where $M = [m_1\ m_2\ \cdots\ m_d]$ is a $d \times d$ integer matrix with m_i as its ith column.

B. Two-Dimensional Separable Wavelets

The 2-D separable wavelet transform [28] is obtained from the tensor product of the corresponding 1-D wavelets. Suppose that $H^{(1d)}(z)$ and $G^{(1d)}(z)$ are 1-D lowpass and highpass decomposition filters, then the lowpass and three highpass channels corresponding to the *Horizontal*, *Vertical*, and *Diagonal* subbands for 2-D wavelets are obtained as Fig. 1(a) illustrates. In this work, we denote the sampling matrix $\mathtt{M}$ as $\mathrm{diag}(2,2) = 2I_2$. Fig. 1(b) shows how the WT[1] partitions the frequency space. Since the WT uses a separable construction, the basis functions are merely aligned in two horizontal and vertical directions [see Fig. 1(c)]. As a result, wavelets have poor directionality.

C. Directional Filter Banks

Bamberger and Smith introduced *directional filter banks* (DFB) using quincunx and parallelogram filter banks [2], [4]. An improved version of the DFB using tree-structured filter banks was developed recently [31]. In an l-level DFB, the frequency space is divided into 2^l wedge-shaped subbands [see Fig. 2(a)]. The overall sampling matrices $D_i^{(l)}$ for channels $1 \le i \le 2^l$ of such a DFB is [31]

$$D_i^{(l)} = \begin{cases} \mathrm{diag}(2^{l-1}, 2), & \text{for } 1 \le i \le 2^{l-1} \\ \mathrm{diag}(2, 2^{l-1}), & \text{for } 2^{l-1} < i \le 2^l \end{cases}$$

[1]From hereafter, we mention 2-D separable wavelet transform as *wavelet transform* (WT).

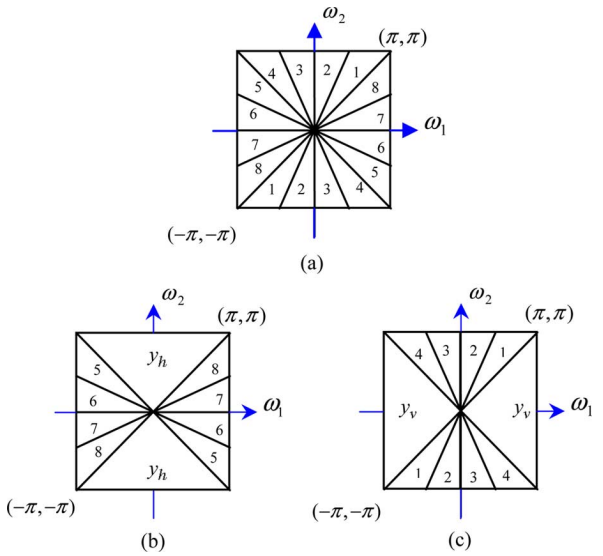

Fig. 2. (a) Frequency response of a (full-tree) DFB decomposed in three levels. (b) An example of the *vertical directional filter bank* (VDFB) using three levels. (c) An example of the *horizontal directional filter bank* (HDFB) using three levels.

where the channels $1 \leq i \leq 2^{l-1}$ correspond to the *mostly horizontal* subbands and the channels $2^{l-1} < i \leq 2^l$ indicate the *mostly vertical* subbands.

We can also construct *half-tree* DFBs by just decomposing the mostly *vertical* directions or the mostly *horizontal* directions, where we call the resulting schemes *vertical DFB* (VDFB) and *horizontal DFB* (HDFB) as Fig. 2 depicts [18]. In VDFB (HDFB), we stop iterating at subband y_h (y_v) after one level and do not decompose the signal horizontally (vertically) further. We call the subbands y_h and y_v as *pseudodirectional* subbands.

The first level of the DFB is a simple *quincunx filter bank* (QFB) with fan filters. Therefore, the overall sampling matrices for VDFB and HDFB are

$$D_i^{V(l)} = \begin{cases} Q, & \text{for subband } y_h (i = \text{`}h\text{'}) \\ \operatorname{diag}(2, 2^{l-1}), & \text{for } 2^{l-1} < i \leq 2^l \end{cases}, \text{ and}$$

$$D_i^{H(l)} = \begin{cases} \operatorname{diag}(2^{l-1}, 2), & \text{for } 1 \leq i \leq 2^{l-1} \\ Q, & \text{for subband } y_v (i = \text{`}v\text{'}) \end{cases}$$

where Q is a quincunx sampling matrix. Note that we number the *directional* channels in the half-tree DFBs similar to a regular DFB. Moreover, we denote the overall reconstruction filters by $F_i^{(l)}(\mathbf{z})$, $(1 \leq i \leq 2^l)$ for the DFB subband i, and also directional subbands in VDFB and HDFB with appropriate i. We also denote the synthesis fan filters resulting in subbands y_h and y_v by $F_h(\mathbf{z})$ and $F_v(\mathbf{z})$, respectively. Then, the functions $\{f_i^{(l)}[\mathbf{n} - D_i^{(l)}\mathbf{m}]\}_{1 \leq i \leq 2^l, \mathbf{m} \in \mathbb{Z}^2}$ (and similarly $\{f_i^{(l)}[\mathbf{n} - D_i^{V(l)}\mathbf{m}]\}_{i \in I_v^{(l)}, \mathbf{m} \in \mathbb{Z}^2}$ and $\{f_i^{(l)}[\mathbf{n} - D_i^{H(l)}\mathbf{m}]\}_{i \in I_h^{(l)}, \mathbf{m} \in \mathbb{Z}^2}$ in VDFB and HDFB, where $I_v^{(l)} = \{i | i = \text{`}h\text{' or } 2^{l-1} < i \leq 2^l\}$ and $I_h^{(l)} = \{i | i = \text{`}v\text{' or } 1 \leq i \leq 2^{l-1}\}$) provide a directional basis for $l^2(\mathbb{Z}^2)$. Note that if we utilize orthogonal fan filters in the DFBs,[2] the basis functions are orthogonal in the corresponding DFB [14].

[2]By DFBs, we sometimes mean both full-tree and half-tree DFBs depending on the context.

Since we use quincunx sampling at the first level, the shape of subbands y_h and y_v in the spatial domain is diamond. We can change the shape into a rectangle using a unimodular matrix and shifting, as explained in [18].

III. Hybrid Wavelets and DFB

A. Construction

We propose to extend the directionality of the WT by employing the DFBs to the highpass channels of the WT. Therefore, we use the name *hybrid wavelets and directional filter banks* (HWD) transform family. Before describing the construction, we elaborate further regarding the proper use of the DFBs in this scheme.

A major drawback of employing DFB is the pseudo-Gibbs phenomena artifacts introduced when some of the transform coefficients are set to zero during NLA, coding [20], and denoising [17]. Since in the DFB we need to use long filters for better directional resolution and since the basis functions are directional, it turns out that the issue of ringing artifacts will be severer for the DFB when compared with other subband schemes such as WT. Do and Vetterli attempted to address this issue by applying the DFB to the Laplacian pyramid in which the highpass channels are free from frequency scrambling [14], [15].

In previous work [20], [21], we applied DFBs to all the highpass channels of WT, which resulted in introducing many artifacts in the smooth regions during NLA and coding. In this work, we address the problem as described below.

Conjecture 1: The main reason for the creation of ringing artifacts when applying the DFB to the WT highpass channels is employing the DFB to the *coarser wavelet subbands*.

This conjecture is based on the following reasons.

1) The human visual system is more sensitive to the low-frequency portions of images. Consequently, the ringing artifacts resulting from the coarser wavelet scales due to applying DFBs render more irritant distortions. In addition, smooth regions have nonzero transform coefficients mainly in the coarser scales of the WT and are best represented by wavelet basis functions. Therefore, it is crucial to retain coarser wavelet subbands and do not change their basis elements.
2) Although the frequency scrambling exists in all the levels of wavelet highpass channels, it is worse for coarser levels due to the lower frequency content of these subbands.
3) Suppose that a line segment of support size of $\ell \times 1$ exists in the input image and we apply a J-level WT (we assign level one to the finest resolution). Then the support size of the line at a level j $(1 \leq j \leq J)$ is approximately $[(1 - 2^{-j})\ell_g + 2^{-j}\ell] \times (1 - 2^{-j})\ell_g$ for the diagonal subband (a similar expression is obtained for other subbands), where ℓ_g is the length of the 1-D highpass filter $g^{(1d)}[n]$. Observe that the line segment becomes thicker in coarser scales. Since we would also have larger directional basis elements if we apply DFB to the coarser scales, we expect introducing more distortion during nonlinear approximation.
4) Since large-size fan filters are employed in the DFB, the size of coarser subbands usually becomes less than the size

of the DFB filters applied to them. In this case, we take advantage of the periodic extension[3] of the signal as we see in the following example. Assume a 1-D N-point signal $x[n]$ and a filter with length ℓ ($N < \ell \leq 2N$) are given. To obtain a filtered signal with size N, we can concatenate two copies of $x[n]$ to obtain $x_C[n]$. Now we can use $2N$-point *discrete Fourier transform* (DFT) [30] to obtain the filtered output $y_C[n]$ and find $y[n]$ as the first N-point of $y_C[n]$. One can prove that the $2N$-point DFT of $x_C[n]$ is expressed as

$$X_C^{(2N)}[k] = \begin{cases} 2X^{(N)}[k] & \text{for } k = 0, 2, \ldots, 2N-2 \\ 0 & \text{for } k = 1, 3, \ldots, 2N-1 \end{cases}$$

where $X^{(N)}[k] = \sum_{n=0}^{N-1} x[n] e^{-jn(2\pi/N)k}$ is the N-point DFT of $x[n]$. Therefore, $X_C^{(2N)}[k]$ is proportional to the concatenation of two copies of $X^{(N)}[k]$ where the odd samples are set to zero. It turns out that a distorted version of the input signal $x[n]$ is employed in filtering, which makes the output distorted. □

Now we explain how to construct the HWD transform family. Since, in the WT, we already have horizontal and vertical subbands, different paradigms could be considered to apply DFBs to the $J_m < J$ finest subbands of wavelets. We propose two types of HWD transforms.

- *HWD Using Both Full-Tree and Half-Tree DFBs (HWD-H).*
  1) Apply *HDFBs* with l_j levels to *vertical* wavelet subbands at levels $1 \leq j \leq J_m$. We denote these subbands by $\mathtt{VD}_j^{(i)}$ ($i \in I_h^{(l_j)} = \{i | 1 \leq i \leq 2^{l_j - 1}$ or $i =$ 'v'$\}$).
  2) Apply *VDFBs* with l_j levels to *horizontal* wavelet subbands at levels $1 \leq j \leq J_m$. We denote these subbands by $\mathtt{HD}_j^{(i)}$ ($i \in I_v^{(l_j)} = \{i | i =$ 'h' or $2^{l_j - 1} < i \leq 2^{l_j}\}$).
  3) Apply (full-tree) *DFBs* with l_j levels to *diagonal* wavelet subbands at levels $1 \leq j \leq J_m$. We denote these subbands by $\mathtt{DD}_j^{(i)}$ ($i \in I_d^{(l_j)} = \{i | 1 \leq i \leq 2^{l_j}\}$).
- *HWD Using Full-Tree DFBs (HWD-F):*[4]
  Apply (full-tree) *DFBs* with l_j levels to all three highpass subbands of wavelets at levels $1 \leq j \leq J_m$. We denote the subbands by $\mathtt{VD}_j^{(i)}$, $\mathtt{HD}_j^{(i)}$, and $\mathtt{DD}_j^{(i)}$ ($i \in I_d^{(l_j)} = \{i | 1 \leq i \leq 2^{l_j}\}$) corresponding to the *vertical*, *horizontal*, and *diagonal* wavelet subbands to which we applied the DFBs.

A schematic diagram of the HWD-H transform is illustrated in Fig. 3. Using the noble identities [38], we can move the DFB filters before downsampling by M in the WT. Consequently, we can find the frequency partitioning by the HWD family as Fig. 4 demonstrates.

Remark 1 (Directional Subbands): In HWD-H, since we apply VDFB to wavelet horizontal subband and HDFB to wavelet vertical subband, we *convert* wavelet horizontal and vertical subbands to mostly vertical and horizontal directional subbands, respectively. However, in HWD-F, we have all set of directions at each wavelet highpass subbands in the finest scales.

[3]Note that if we use linear-phase filters, we can benefit from symmetric extension yielding less border artifact.

[4]We formerly called HWD-F and HWD-H as HWD type 3 and HWD type 2, respectively [19].

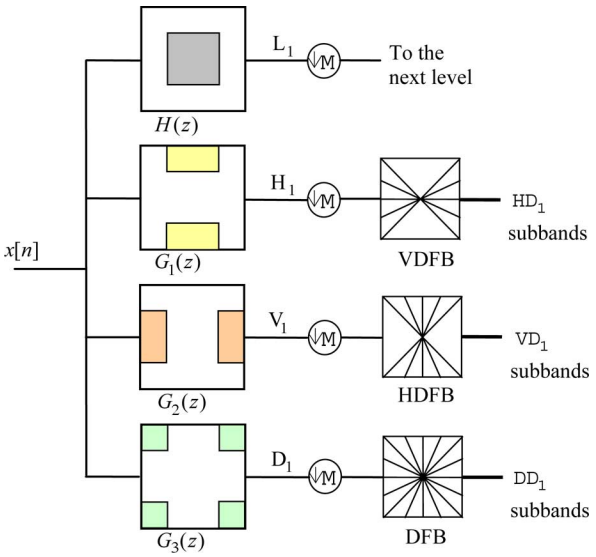

Fig. 3. Schematic plot of the HWD-H transform using $l_1 = 3$ directional levels.

Similar to the DFB, the major direction represented by each directional subband in HWD is perpendicular to the major axis passing through the subband (in the Fourier domain) as Fig. 5 shows. As seen, a directional subband in the wavelet vertical subband represents a mostly horizontal direction (see also Fig. 7).

Remark 2 (Frequency Scrambling): Since our objective is the construction of a critically sampled scheme, we cannot avoid subsampling in the wavelet stage of the HWD transforms. As a result, frequency scrambling in the wavelet highpass subbands is inevitable. That is, the frequency regions of wavelet highpass subbands are subject to stretching and displacement due to downsampling by M. For instance, as Fig. 6 shows, the high-frequency regions (frequencies near $\omega_2 = \pi$) of the horizontal wavelet subband are mapped to low-frequency regions (frequencies near $\omega_2 = 0$) after downsampling. Therefore, to decrease the aliasing due to downsampling, in HWD-H we decompose horizontal wavelet subbands (at finest scales) into mostly vertical directions (see Fig. 6) and vertical wavelet subbands into mostly horizontal directions. Nonetheless, for some images with a large amount of textures and oscillatory patterns, taking advantage of full-tree DFBs in all wavelet finest subbands as in HWD-F, yields better results indicating the minor impact of the frequency scrambling in this case.

In Fig. 7, we show some basis functions of the HWD family in both the space and Fourier domains (note that the Fourier transform of a basis function corresponds to its relevant subband). As a matter of fact, in the HWD family, we convert the wavelet basis functions at a few finest scales to *more directional* basis elements. We also show a few basis functions of the DFB in Fig. 7(c).

Remark 3: Note that under HWD-F, since some of the DFB filters are oriented similar to the wavelet subbands, we have more aliasing. Additionally, from Fig. 7(b) last row, we can see that since the wavelet filters fail to perfectly separate frequency regions, we have more leakage to low-frequency region in those

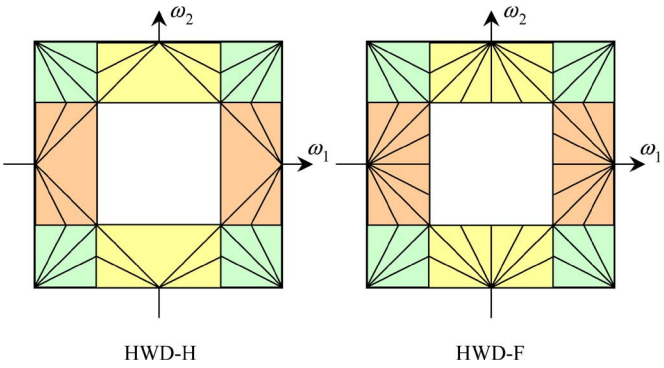

Fig. 4. Frequency partitioning in the HWD family using $l_1 = 3$ directional levels.

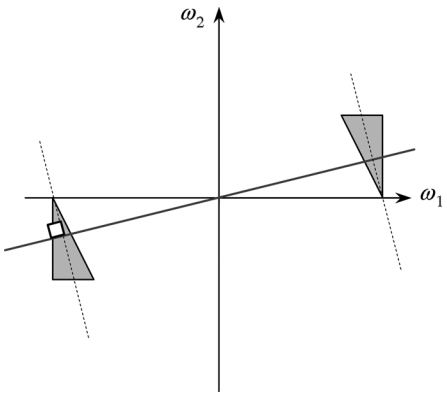

Fig. 5. *Directional* subband of HWD ($\mathtt{VD}_1^{(3)}$). The shaded regions show the frequency support of the subband and the solid line indicate its major direction in the space domain.

subbands. Therefore, there exists a rather significant frequency aliasing in some of the directional subbands of HWD-F where it is a major cause of artifacts during applications when a number of coefficients are set to zero.

Remark 4: As mentioned in Remark 1, the major direction represented by each directional subband in HWD is the same as the direction of the DFB subband that is employed in the HWD subband. As a result, all three directional subbands $\mathtt{VD}_j^{(i)}$, $\mathtt{HD}_j^{(i)}$, and $\mathtt{DD}_j^{(i)}$ represent the same direction as subband i of the DFB stands for (see Fig. 2). We can see this fact from Fig. 7 when we compare (a) and (c).

Note that both stages utilized in the HWD family (i.e., the WT and DFB) are nonredundant and we can use any number of directions in this construction. Consequently, the HWD transforms provide a family of nonredundant, flexible, and rich *directional* and *nondirectional* basis elements leading to good NLA decay for natural images, as we demonstrate in Section V.

B. HWD for Quincunx Wavelets

Similar to the HWD, we can add directionality to the *quincunx wavelet transform* (QWT) to construct *hybrid quincunx wavelets and directional filter banks* (HQWD). In contrast to the WT, the QWT uses nonseparable diamond filters and has just one highpass channel at each level. As a result, we propose the HQWD transform as follows [see Fig. 8(a)].

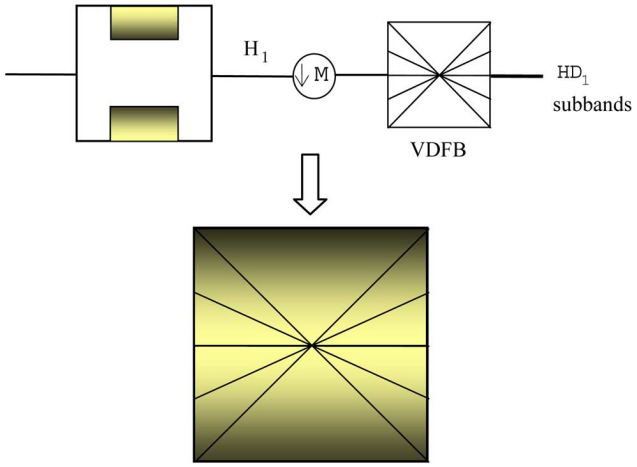

Fig. 6. Effect of downsampling on the wavelet highpass subband which gives rise to frequency scrambling. By applying VDFB to horizontal subband in the HWD-H scheme, one can avoid inputting low-frequency regions of the wavelet subband to the directional decomposition.

- *HQWD*:
  Apply (full-tree) *DFBs* with l_j levels to the highpass subbands of quincunx wavelets at levels $1 \le j \le J_m$. We denote the resulting subbands by $\mathtt{QD}_j^{(i)}$ $(1 \le i \le 2^{l_j})$.

Again, after using the noble identities, the frequency span of the HQWD is obtained as Fig. 8(b) shows. A few basis functions are depicted in Fig. 8(c). We consider the following quincunx sampling matrices for odd and even QWT levels, respectively

$$Q_1 = \begin{bmatrix} 1 & 1 \\ -1 & 1 \end{bmatrix}, \quad \text{and} \quad Q_2 = \begin{bmatrix} 1 & -1 \\ 1 & 1 \end{bmatrix}.$$

In this case, at even levels (i.e., $j = 2k$, $k \in \mathbb{Z}$) we have the equivalent overall sampling of $\mathtt{M}^{(j/2)}$.

C. Scaling Law and DFB Levels

Suppose that, in HWD, we apply l_j-level DFBs to the highpass subbands of level j in the WT. Then a transform coefficient in the directional subbands of the HWD will have support size of about $2\ell_f \times 2^{l_j-1}\ell_f$ after the DFB reconstruction, where the maximum size of the fan filter pair of the DFB are assumed (ℓ_f, ℓ_f). Now, to obtain the basis element, we pass the resulting coefficients through j-level WT synthesis bank. Therefore, we have an upsampling by $\mathtt{M}^j$, which expands the size of the input by $2^j \times 2^j$ followed by filtering by the overall synthesis filters of size about $(2^j - 1)\ell_g \times (2^j - 1)\ell_g$. As a result, the support size of the basis elements in the directional subbands of the HWD family is about $2^{j+1}\ell_1 \times 2^{l_j+j-1}\ell_2$, where $\ell_1 \approx \ell_2$ are constants.

Consequently, similar to contourlets, we can hold the *parabolic scaling law* of $width \propto length^2$ [8], [15] through decreasing the directional levels l_j at every other coarser wavelet scales up to level J_m : $l_{j_2} = l_{j_1} - \lfloor (j_2 - j_1)/2 \rfloor$, for levels $1 \le j_1 < j_2 \le J_m$.

Note that, in the case of the HQWD, the QWT synthesis bank involves upsampling by Q^j that is equal to $\mathtt{M}^{j/2}$. Hence, the support size of the basis elements in HQWD is about $2^{j/2+1}\ell_1 \times$

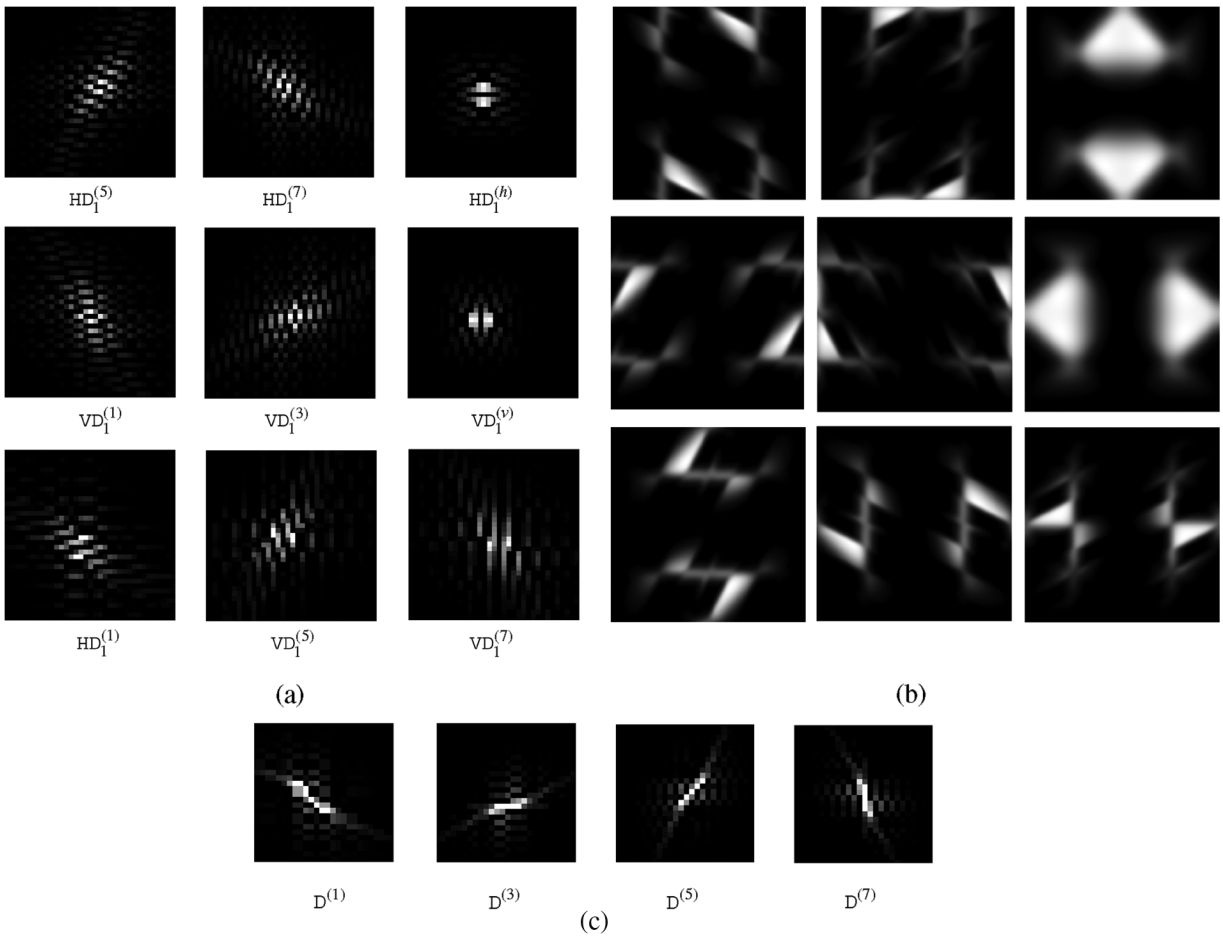

Fig. 7. (a) Some *directional* basis functions of the HWD-H (first two rows of which the last column corresponds to the pseudodirectional subbands) and HWD-F (all except the pseudodirectional ones) when $l_1 = 3$ (only positive values are shown). (b) The corresponding magnitudes of the Fourier transform of the basis functions in (a). (c) Four basis functions of the DFB with $l = 3$.

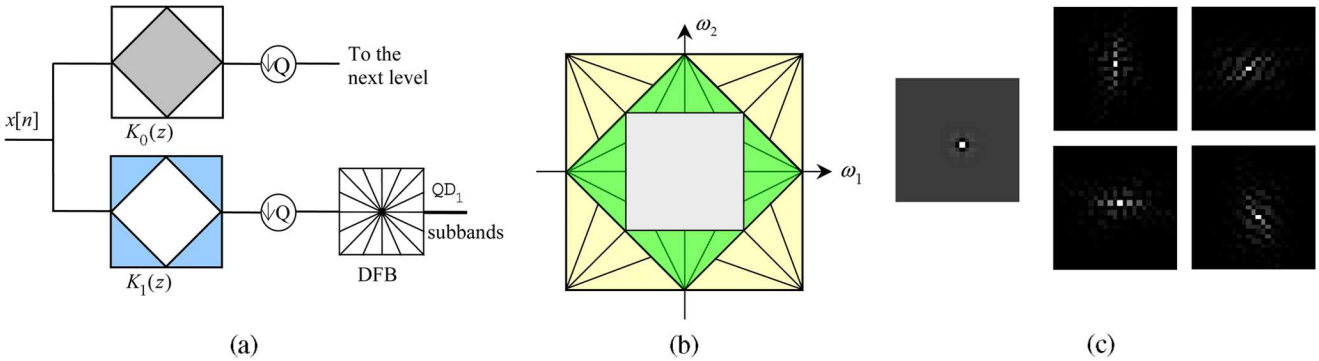

Fig. 8. (a) HQWD transform. (b) The frequency partitioning in the HQWD with $l_1 = l_2 = 3$ directional levels. (c) *Left*: A basis function of the QWT. *Right*: Some directional basis functions of HQWD.

$2^{l_j+j/2-1}\ell_2$ ($\ell_1 \approx \ell_2$). It follows that for the HQWD transform, we should enforce the scaling rule

$$l_{j_2} = l_{j_1} - \lfloor (j_2 - j_1)/4 \rfloor, \quad (1 \le j_1 < j_2 \le J_m).$$

The number of directions in the DFB stage (l_j) and the number of finest wavelet scales (J_m) that should be employed in the HWD are dependent on the image size and the amount of textures in the image. For texture images and images with a significant amount of texture regions we use larger values of directional levels. To satisfy item 3 in Conjecture 1 for a given image of size $N \times N$ and fan filter pair of the DFB with maximum support size of (ℓ_f, ℓ_f), we should have

$$J_m < \log_2 \frac{N}{2\ell_f}$$

where l_{J_m} is assumed 2 (the minimum number of directional levels). Note that, for HQWD, we have $J_m < 2\log_2(N/2\ell_f)$.

IV. Analysis and Realization

A. Multiresolution Analysis

Having the multiresolution framework for 2-D separable wavelets, we extend it to a new system to account for the proposed schemes.

Suppose that we construct 2-D wavelets from 1-D scaling and wavelet functions (φ and ψ) as [28]

$$\begin{aligned}\psi^1(\mathbf{t}) &= \varphi(t_1)\psi(t_2)\\ \psi^2(\mathbf{t}) &= \psi(t_1)\varphi(t_2), \quad \text{and}\\ \psi^3(\mathbf{t}) &= \psi(t_1)\psi(t_2)\end{aligned}$$

which form an orthonormal basis of $\mathbf{L}^2(\mathbb{R}^2)$. The 2-D multiresolution is defined as $\mathbf{V}_j^2 = \mathbf{V}_j \otimes \mathbf{V}_j, (j \in \mathbb{Z})$, where $\{\mathbf{V}_j\}_{j\in\mathbb{Z}}$ denotes the corresponding 1-D approximation space and we have the detail space $\mathbf{W}_j^2$ connected to the approximation space as the orthogonal component of $\mathbf{V}_j^2 : \mathbf{V}_{j-1}^2 = \mathbf{V}_j^2 \oplus \mathbf{W}_j^2$. The approximation spaces have the inclusion property of $\mathbf{V}_{j+1}^2 \subset \mathbf{V}_j^2, (j \in \mathbb{Z})$. Defining the 1-D wavelet at scale 2^j as $\{\psi_{j,n}(t) = 2^{-j/2}\psi(2^{-j}t - n)\}_{j,n\in\mathbb{Z}}$, the family $\{\psi_{j,\mathbf{n}}^k(\mathbf{t})\}_{\substack{\mathbf{n}\in\mathbb{Z}^2\\ 1\le k\le 3}}$ is an orthonormal basis of $\mathbf{W}_j^2$. Note that we can also define the detail orthogonal subspaces $\mathbf{W}_j^{2,1} = \mathbf{V}_j \otimes \mathbf{W}_j$, $\mathbf{W}_j^{2,2} = \mathbf{W}_j \otimes \mathbf{V}_j$, and $\mathbf{W}_j^{2,3} = \mathbf{W}_j \otimes \mathbf{W}_j$, where $\mathbf{W}_j^2 = \oplus_{k=1}^3 \mathbf{W}_j^{2,k}$.

Now, for instance, we consider the HWD-H transform, where we apply l_j-level ($j \le J_m$) DFBs to the detail multiresolution space $\mathbf{W}_j^2$ as (see Section II-C)

$$\eta_{i,j,\mathbf{n}}^{1,(l_j)}(\mathbf{t}) = \sum_{\mathbf{m}\in\mathbb{Z}^2} f_i^{(l_j)}\left[\mathbf{m} - D_i^{V(l_j)}\mathbf{n}\right]\psi_{j,\mathbf{m}}^1(\mathbf{t}), \quad \text{for} \quad i \in I_v^{(l_j)}$$

$$\eta_{i,j,\mathbf{n}}^{2,(l_j)}(\mathbf{t}) = \sum_{\mathbf{m}\in\mathbb{Z}^2} f_i^{(l_j)}\left[\mathbf{m} - D_i^{H(l_j)}\mathbf{n}\right]\psi_{j,\mathbf{m}}^2(\mathbf{t}), \quad \text{for} \quad i \in I_v^{(l_j)}$$

and

$$\eta_{i,j,\mathbf{n}}^{3,(l_j)}(\mathbf{t}) = \sum_{\mathbf{m}\in\mathbb{Z}^2} f_i^{(l_j)}\left[\mathbf{m} - D_i^{(l_j)}\mathbf{n}\right]\psi_{j,\mathbf{m}}^3(\mathbf{t}) \quad \text{for} \quad 1 \le i \le 2^{l_j} \left(\text{or} \quad i \in I_d^{(l_j)}\right).$$

Therefore, by using orthogonal DFBs, we span the detail subspaces $\mathbf{W}_j^{2,1}$, $\mathbf{W}_j^{2,2}$, and $\mathbf{W}_j^{2,3}$ ($j \le J_m$) into the following orthogonal directional subspaces:

$$\begin{aligned}\mathbf{W}_j^{2,1} &= \bigoplus_{i\in I_v} \mathbf{W}_j^{2,1,(i)}\\ \mathbf{W}_j^{2,2} &= \bigoplus_{i\in I_h} \mathbf{W}_j^{2,2,(i)}, \quad \text{and}\\ \mathbf{W}_j^{2,3} &= \bigoplus_{i\in I_d} \mathbf{W}_j^{2,3,(i)}.\end{aligned}$$

For the other levels $J_m < j \le J$ in HWD-H, we have the same functions as wavelets $\{\psi_{j,\mathbf{n}}^k(\mathbf{t})\}_{\substack{\mathbf{n}\in\mathbb{Z}^2\\ 1\le k\le 3}}$.

Remark 5: The family $\{\eta_{i_1,j,\mathbf{n}}^{1,(l_j)}, \eta_{i_2,j,\mathbf{n}}^{2,(l_j)}, \eta_{i_3,j,\mathbf{n}}^{3,(l_j)}\}_{\substack{i_1\in I_v, i_2\in I_h, i_3\in I_d\\ \mathbf{n}\in\mathbb{Z}^2}}$ provides an orthonormal basis for $\mathbf{W}_j^2$ ($j \le J_m$). In addition, each individual family $\{\eta_{i_1,j,\mathbf{n}}^{1,(l_j)}\}_{\substack{i_1\in I_v\\ \mathbf{n}\in\mathbb{Z}^2}}$, $\{\eta_{i_2,j,\mathbf{n}}^{2,(l_j)}\}_{\substack{i_2\in I_h\\ \mathbf{n}\in\mathbb{Z}^2}}$, and $\{\eta_{i_3,j,\mathbf{n}}^{3,(l_j)}\}_{\substack{i_3\in I_d\\ \mathbf{n}\in\mathbb{Z}^2}}$ provides an orthonormal basis for the detail subspaces $\mathbf{W}_j^{2,1}$, $\mathbf{W}_j^{2,2}$, and $\mathbf{W}_j^{2,3}$ ($1 \le j \le J_m$), respectively.

Proof of the above statement is similar to that of the quadtree decomposition in wavelet packets [28]. Since we use orthonormal filters in the DFBs, we divide $\mathbf{W}_j^{2,k}$, ($1 \le k \le 3$) into orthogonal detail subspaces after each directional level. As a result, the proof is achieved through induction.

Remark 6: The family $\{\eta_{i_1,j,\mathbf{n}}^{1,(l_j)}(\mathbf{t}), \eta_{i_2,j,\mathbf{n}}^{2,(l_j)}(\mathbf{t}), \eta_{i_3,j,\mathbf{n}}^{3,(l_j)}(\mathbf{t})\}_{\substack{i_1\in I_v, i_2\in I_h, i_3\in I_d\\ \mathbf{n}\in\mathbb{Z}^2, j\le J_m}}$ together with $\{\psi_{j,\mathbf{n}}^k(\mathbf{t}), \varphi_{J,\mathbf{n}}(\mathbf{t})\}_{\substack{\mathbf{n}\in\mathbb{Z}^2, J>j>J_m\\ 1\le k\le 3}}$ provide an orthonormal basis for $\mathbf{L}^2(\mathbb{R}^2)$.

We can derive similar analyses for HWD-F and also HQWD.

B. Approximation

Owing to the similar structure of the proposed HWD-F to contourlets [15], one can prove a similar NLA rate of decay for HWD-F for a class of signals. In particular, it can be shown that an image x containing $\boldsymbol{C}^2$ regions separated by $\boldsymbol{C}^2$ curves when decomposed by an HWD-F transform, follows the NLA decay of

$$\|x - x_M\|_2^2 \le A(\log M)^3 M^{-2}$$

where x_M is the reconstructed image using M largest-magnitude transform coefficients and A is a positive constant. Note that the directional subbands in the HWD-F transform should have as many directional vanishing moments as possible (ideally have perfect *flat* passbands and are zero elsewhere) and the wavelet scaling function should satisfy $\varphi \in \boldsymbol{C}^2$.

The proof is similar to the one provided for the contourlet transform's approximation decay [15]; however, we must emphasize a few points.

1) Generally, the curves in the image will have components in all three wavelet highpass subbands where they are subject to being directionally decomposed by the DFBs. Thus, each segment of curve will have just significant components when it intersects a directional basis function oriented alongside the curve. The fact that we have three highpass channels in the WT stage of HWD as opposed to the one highpass subband of the pyramid stage of contourlets, only changes the constant A in the NLA decay rate.
2) The scales $j > J_m$ (wavelet subbands) in HWD-F mostly stand for the smooth regions and the wavelet highpass subbands furnish sufficient angular resolution for the curve components (we assume that J_m is large enough to cover all *fine* scales of the WT).
3) Unlike the contourlet transform, since HWD take advantage of wavelets with horizontal and vertical vanishing moments and good NLA decay when compared with the Laplacian pyramid in contourlets, HWD practically shows better NLA decay in comparison to the contourlet transform (see Section V-A).

In the next section, we provide an efficient realization for the proposed transform family.

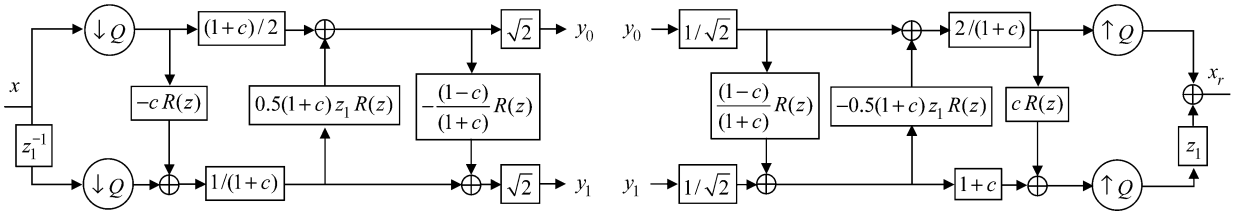

Fig. 9. *Left:* Analysis bank of the triplet QFB. *Right:* The synthesis bank.

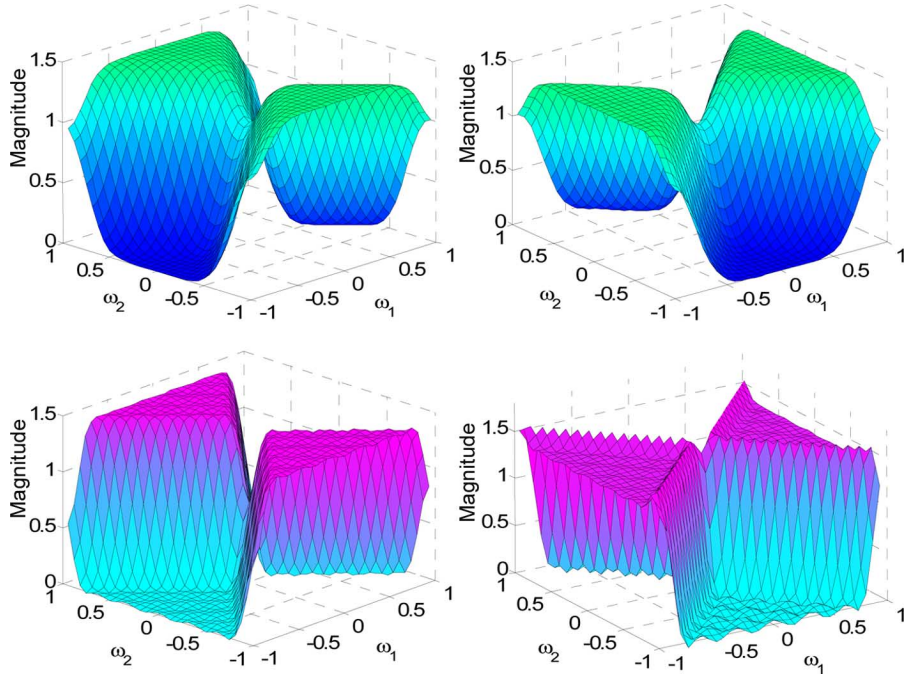

Fig. 10. *Top:* Fan filter pair using triplet filter bank [1]. *Bottom:* The fan filter pair using double-halfband filter bank [32].

C. Efficient Realization

While the WT can be implemented efficiently using 1-D filters, the DFBs in the HWD need to be treated carefully. Although the quincunx filter bank [38], which is the major building block of a DFB, is a nonseparable filter bank system, it is possible to implement it using ladder network and, hence, benefiting from low computational cost similar to 2-D separable filtering.

Phoong *et al.* [32] proposed a two-channel filter bank using a pair of halfband filters, which can be realized in the polyphase domain using ladder network. This scheme, however, has some restrictions. Ansari *et al.* [1] proposed a two-channel filter bank using a triplet of halfband filters, where they could address the restrictions in double-halfband filter bank. We use this scheme to construct the DFBs.

The equivalent analysis band of the *quincunx filter bank* (QFB) scheme using diamond filter is shown in Fig. 9. The parameter c is set to $\sqrt{2}-1$, to ensure that the 1-D lowpass and highpass filters have the same magnitude of $1/\sqrt{2}$ at $\omega=\pi/2$; a condition not achieved using the double-halfband filter bank. To have the maximum regularity of the filters, we use the Lagrange coefficients (a_k) in the FIR 1-D T-filter [1] $R^{(1d)}(z)=\sum_{k=1}^{N_T} a_k(z^{-k}+z^{k-1})$, where

$$a_k=\frac{(-1)^{k+N_T-1}\prod_{i=1}^{2N_T}(N_T+0.5-i)}{(N_T-k)!(N_T-1+k)!(k-0.5)}.$$

To have a QFB with diamond filter pair, we use the transformation $R(\mathbf{z})=R^{(1d)}(z_1)R^{(1d)}(z_2)$, whereas we use time-reversed versions of the T-filters to obtain a QFB with fan filters: $R(\mathbf{z})=R^{(1d)}(-z_1)R^{(1d)}(-z_2)$. The resulting filter pair will have support sizes of $(8N_T-3, 8N_T-3)$ and $(12N_T-5, 12N_T-5)$.

Fig. 10 depicts the frequency responses of the fan filter pairs using both double-halfband [with support size of (23, 23) and (45, 45)] and triple-halfband [with support size of (29, 29) and (43, 43)] ladder structures. It is clear that the triplet filter bank yields smoother fan filters and consequently introduces less visible ringing artifacts when employed in the DFBs.

One of the issues affecting the efficiency of a transform is the regularity of its filters [24]. Since HWD is composed of two filter bank stages, its regularity is dependent on the regularity of both wavelets and DFBs. While the regularity of DFBs needs a comprehensive treatment, here we resort to performing a simple test. The largest first-order difference of the coefficients of the iterated filter bank in the lowpass channel (which leads to an approximate of the scaling function) is an indication of the regularity [24], [25]. Here we measure the largest first-order difference when we apply an l-level DFB to the wavelet scaling function. We approximate φ by seven iterations of the Daubecheis 9/7 analysis filter and apply both double- and tipple-halfband DFBs with *normalized* filters and l levels to φ. Table I shows

TABLE I
LARGEST FIRST-ORDER DIFFERENCE OF THE DFB WHEN APPLIED TO φ

DFB level (l)	No DFB	2	3	4
DFB (THF)[1]	0.0239	0.0245	0.0320	0.0431
DFB (DHF)[2]	0.0239	0.0466	0.0815	0.1479

[1]DFB using normalized triple-halfband filters
[2]DFB using normalized double-halfband filters

the maximum value of the first-order differences obtained for all the DFB subbands in the n_1 and n_2 directions. As seen and expected, it is clear that the DFB with triple-halfband filters has more regularity.

In what follows, we examine the complexities of the proposed schemes.

D. Complexity

Since the HWD transforms are composed of two stages, we first express the complexities of wavelets and DFBs. Here we evaluate the complexities of the analysis banks; similar expressions for the synthesis banks can be derived.

1) WT: Suppose that we use analysis 1-D filters of a same even length, ℓ_h, in the 2-D WT. Then the complexity of a *single-level* WT is $2\ell_h$ *multiplications per input sample* (MPS) and $2\ell_h - 2$ *additions per input sample* (APS). If we use *linear-phase* filters, we have ℓ_h MPS and $2\ell_h - 2$ APS in the WT. For an *octave-band* WT, the complexity will be up to 4/3 times the complexity of a single-level WT [41].
2) DFB: Regarding the ladder network shown in Fig. 9, the complexity of the QFB is evaluated as follows. Since at each channel we decrease the number of samples by 2 and we have three levels of separable convolution with 1-D T-filters having a length of ℓ_r, the complexity of the QFB is $3\ell_r + 1$ MPS and $3\ell_r - 3/2$ APS. For the *linear-phase* maximally flat filters that we use in this work, we have $3N_T + 1$ MPS and $3N_T - 3/2$ APS ($N_T = \ell_r/2$) for the QFB. For a J-level octave-band QWT, we have $2(1-1/2^J)$ times the complexity of the QFB.
The complexity of an l-level DFB is l times that of the QFB (note that after each level the size of the signal is halved). A half-tree DFB needs $(l+1)/2$ times the operations required for the QFB.
3) HWD: Suppose that in the HWD (considering linear-phase filters), we apply l_j-level DFBs ($1 \le j \le J_m$) to the jth highpass channels of the WT. Then the complexity of HWD-F is about

$$(4/3)\ell_h + 3(3N_T+1)\sum_{j=1}^{J_m}(l_j/4^j)\ \text{MPS} \quad \text{and}$$

$$(4/3)\ell_h + 9(N_T-1/2)\sum_{j=1}^{J_m}(l_j/4^j)\ \text{APS}.$$

In the case of HWD-H, the complexity is about

$$(4/3)\ell_h + (3N_T+1)\sum_{j=1}^{J_m}\left((2l_j+1)/4^j\right)\ \text{MPS} \quad \text{and}$$

$$(4/3)\ell_h + 3(N_T-1/2)\sum_{j=1}^{J_m}\left((2l_j+1)/4^j\right)\ \text{APS}$$

and for the HQWD, we have

$$(3N_T+1)\left(2(1-1/2^J)+\sum_{j=1}^{J_m}(l_j/2^j)\right)\ \text{MPS} \quad \text{and}$$

$$3(N_T-1/2)\left(2(1-1/2^J)+\sum_{j=1}^{J_m}(l_j/2^j)\right)\ \text{APS}.$$

V. APPLICATIONS AND RESULTS

In this section, we show examples of the HWD transforms and then present potential applications of the proposed transforms. Particularly, we examine their applications in nonlinear approximation, image coding, and image denoising.

Fig. 11 depicts two examples of the HWD transforms of the *Barbara* and *Boats* images. In Fig. 11, the wavelet subbands are separated with white lines and the directional subbands at the two finest wavelet subbands are separated with gray lines. The transform coefficients are clipped for better visualization.

A. Nonlinear Approximation

Nonlinear approximation (NLA) is an efficient approach to measure the capability of a transform in sparse representation of a signal. Having a good NLA behavior, a transform would have potential in several signal processing applications such as coding, denoising, and feature extraction.

We tested our proposed transforms using a variety of images and compared them with other transforms such as the WT and contourlets [15]. We used five decomposition levels in all methods and employed Daubechies 9/7 filters for the WT. For the HWD transforms we set $J_m = 2$. For contourlets, we used $\{l_j\}_{1\le j\le 5} = \{5,4,4,3,3\}$ ($j = 1$ corresponds to the finest scale) directional levels. Fig. 12 shows two examples of the NLA PSNR results versus the number of retained coefficients. For the *Barbara* image, we used HWD-F with $l_1 = l_2 = 3$ directional levels, while for the *Peppers* image (and other images that contain less texture), we used HWD-H with $l_1 = l_2 = 2$.

The proposed HWD transform shows promising results for the *Barbara* image (and other images with significant texture content) where it consistently outperforms both wavelets and contourlets. In particular, it achieves up to 1.6 dB (1.2 dB) improvement over the WT (contourlet transform). In the case of the *Peppers* image, the HWD transform provides comparable result to that of wavelets. Note that for many other images such as *Boats*, *Fingerprint*, *GoldHill*, *Mandrill*, and texture images our experiments indicated that HWD always provides better NLA performance.

Some numerical values for the NLA of the *Barbara* image are also given in Table II. To demonstrate the effect of employing regular fan filters in HWD, we also provided the HWD results when using double-halfband filters. The superior results especially for large values of M are clear for the HWD transform using maximally flat triple-halfband fan filters.

Fig. 13 shows the visual results of NLA of the *Barbara* image when $M = 8192$. As seen, the proposed HWD method provides better detail in conjunction with an acceptable level of artifacts in the result.

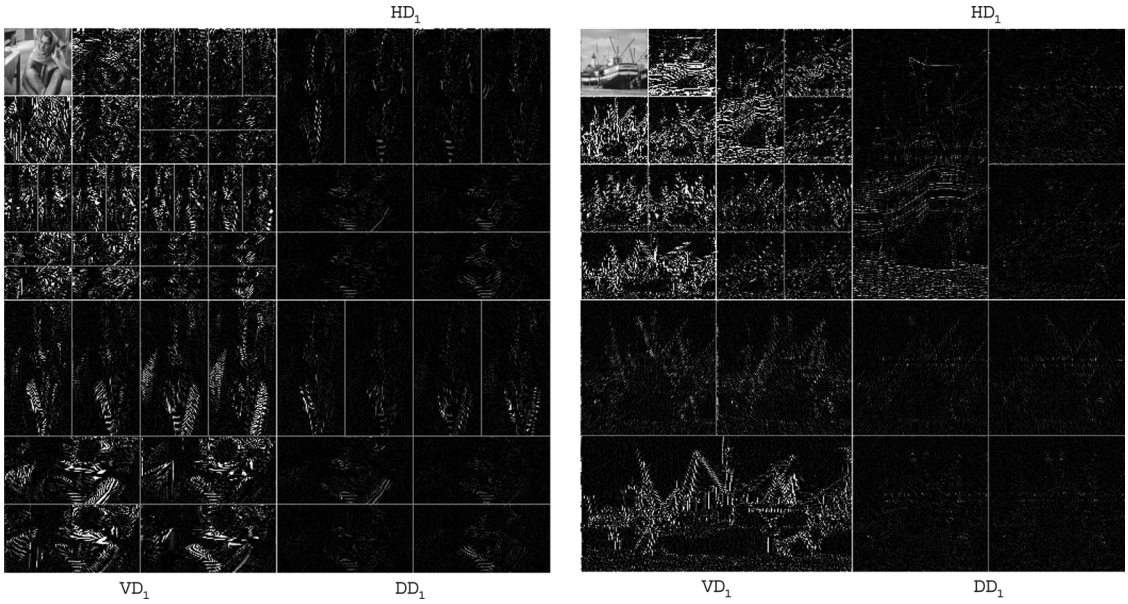

Fig. 11. *Left*: HWD-F transform of the *Barbara* image. Here, $J = 3$, $J_m = 2$, and $l_1 = l_2 = 3$. *Right*: HWD-H transform of the *Boats* image with $J = 3$, $J_m = 2$, and $l_1 = l_2 = 2$.

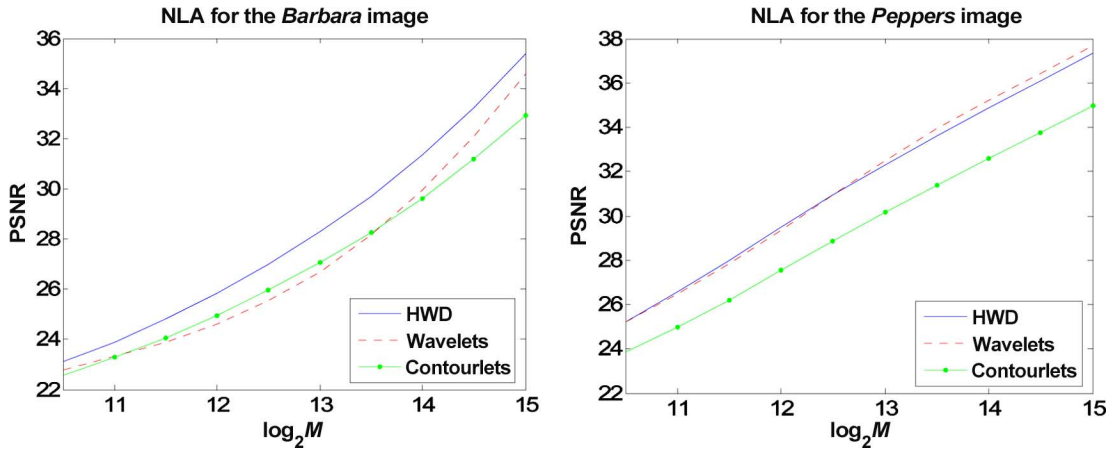

Fig. 12. Examples of the nonlinear approximation PSNR results. *Left*: NLA results for the *Barbara* image. *Right*: NLA results for the *Peppers* image.

TABLE II
PSNR VALUES OF THE NLA EXPERIMENT FOR THE *BARBARA* IMAGE

Method / M	2048	4096	8192	16374	32768
HWD (THF)[1]	**23.91**	**25.86**	**28.28**	**31.35**	**35.39**
HWD (DHF)[2]	23.87	25.73	28.05	30.95	34.73
Wavelets	23.33	24.63	26.68	29.95	34.58
Contourlets [15]	23.29	24.95	27.08	29.63	32.91

[1]HWD using triple-halfband filters for the DFB
[2]HWD using double-halfband filters for the DFB

Our experiments implied that the HWD-H is more appropriate for images that are mostly smooth, whereas HWD-F provides very good performance for images containing a significant amount of fine textures.

We also performed NLA for the HQWD transform and compared it with the quincunx wavelet transform. Table III shows the PSNR values obtained for the *Barbara* image. As seen, HQWD provides a growing improvement in the PSNR values as the number of retained coefficients increases. In this experiment, we used ten wavelet levels, and for the HQWD, we used $J_m = 4$ and $l_j = 3\ (1 \leq j \leq J_m)$.

B. Image Coding

Due to the good NLA performance of the HWD family, and since this transform family is nonredundant, a potential key application for the proposed transforms is image coding.

Although the NLA decay rate of wavelets for images is suboptimal, one can benefit from tree-based coding schemes to improve this decay rate [11]. The SPIHT algorithm is an efficient tree-based wavelet coding scheme [35]. In this scheme, interscale dependencies are considered through the parent–children relationships existing among the wavelet coefficients. Note that although there are other superior schemes such as space-frequency quantization [43] and WSFQ [42], since the scope of this paper is not image coding, we just provide our preliminary results using SPIHT coding algorithm.

To take advantage of the SPIHT scanning algorithm for the HWD transform coefficients, a new parent–children relationship

Fig. 13. Example of the NLA visual results for the *Barbara* image when $M = 8192$.

TABLE III
PSNR VALUES OF THE NLA EXPERIMENT FOR THE *BARBARA* IMAGE (QUINCUNX CASE)

Method / M	2048	4096	8192	16374	32768
HQWD	**22.21**	**23.69**	**25.59**	**28.18**	**31.90**
Quincunx WT	21.95	23.06	24.54	26.64	30.06

should be considered. Suppose that we have an HWD transform with J levels. For the levels $J_m < j \leq J$, we have the same relationship as the one in the WT, and for the levels $1 \leq j \leq J_m$, for each subband $\mathtt{HD}_j$, $\mathtt{VD}_j$, and $\mathtt{DD}_j$ we can use a similar parent–children relationship as the one considered for the contourlet coefficients [33]. The problem appears when we attempt to define the children of coefficients lying at level $J_m + 1$. By applying DFBs to level J_m, we almost remove the interscale dependencies that existed between wavelet levels J_m and $J_m + 1$. Nevertheless, we employ a suboptimal but simple rearrangement algorithm to be able to apply a similar SPIHT scanning algorithm as the one we use for wavelets (seeAppendix I for details).

Although the described procedure is not optimal, we will show that the low bit-rate SPIHT coding results are rather promising for images with high amount of textures and details, where we could capture more details in the HWD coded images when compared with the wavelet coder. In our coding simulation, we used the image *Barbara* and an image composed of 16 textures [5]. For both images we used HWD-F with five wavelet levels and $J_m = 2$, where for the *Barbara* image we used $l_1 = l_2 = 3$ directional levels and $l_1 = l_2 = 4$ directional levels for the *Texture16* image. The number of directional levels is handy optimized.

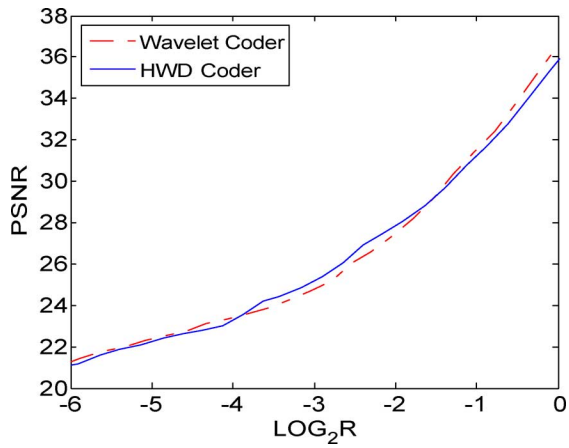

Fig. 14. Coding performance of the wavelet and HWD coders using SPIHT algorithm in terms of PSNR versus the rate for the *Barbara* image.

In Fig. 14, we show the RD curves of the wavelet and proposed coding schemes for the *Barbara* image. As seen, our method provides better or comparable result for a wide range of low bitrate when compared with the wavelet SPIHT coder. Remarkably, unlike the NLA performance of HWD in comparison to that of wavelets, the coding performance does not show significant improvement, which indicates a need for more sophisticated algorithms that we would address later.

Fig. 15 shows visual coding results of the *Barbara* image at 0.25 bpp and the results for *Texture16* at 0.1 bpp are depicted in Fig. 16. As can be seen from the figures, more directional features are retained when using the HWD transform (for example table cover and chair in Fig. 15). Further, we have improved PSNR values compared with those of the wavelet coder.

Wavelets/SPIHT; PSNR = 27.45 HWD-F/SPIHT; PSNR = 27.83

Fig. 15. Coding results of the *Barbara* image at rate 0.25 bpp.

Original Wavelets/SPIHT; PSNR = 18.07 HWD-F/SPIHT; PSNR = 18.22

Fig. 16. Coding results of the *Texture16* image at rate 0.1 bpp.

C. Image Denoising

Image denoising is another application of the HWD transforms. We tested the proposed transforms for denoising of noisy images corrupted with additive white Gaussian noise. For the first part of simulation, we used a simple hard-thresholding rule to shrink the transform coefficients. This way, we can observe to what extent the transform is efficient without the use of more complex shrinkage schemes. The threshold is selected as 3σ [28] where σ is the standard deviation of the input noise and is estimated using robust median estimator [16]. We also mirror extended the images to remedy boundary artifacts. Although the sizes of the noisy images are rather large, the PSNR values of the denoising results change slightly (usually up to ± 0.1 dB) when we use a different noise instance. Hence, to obtain more accurate PSNR values, we repeated each denoising experiment ten times and found the average PSNR values. We also clipped the noisy images to set the pixel values in the allowable range of 0 to 255.

Since the HWD transforms are shift variant, they introduce many artifacts in the denoising results. Therefore, we also constructed *translation-invariant* HWD (TIHWD) transforms by removing subsampling operations to improve the results. A delicate point in developing the TIHWD schemes, is that we should not change the frequency partitioning of the HWD transforms (see Fig. 4). As a result, we first upsample the DFB filters at level j $(1 \leq j \leq J_m)$ by $\mathtt{M}^j$, where $\mathtt{M} = \mathrm{diag}(2,2)$ and then remove the sampling operations using the *generalized algorithme à trous* introduced in [17]. The redundancy ratio of the TIHWD-F is $1 + 3(J - J_m) + 3\sum_{j=1}^{J_m} 2^{l_j}$ and that of the TIHWD-H is found to be $1 + 3J - J_m + \sum_{j=1}^{J_m} 2^{l_j+1}$.

In addition to the proposed methods, we also employed the *wavelet transform* (WT), *contourlet transform* (CT) [15], and adaptive wiener filter using "wiener2" function in Matlab. Moreover, we used the *curvelet transform via frequency wrapping* (CuTFW) with curvelets at the finest scale [7] (where we found that it gives better denoising results than curvelets via unequispaced FFT approach), *translation-invariant WT* (TIWT) [12], *dual-tree complex wavelet transform* (DTCWT) [23], and *translation-invariant CT* (TICT) [17] using hard thresholding for the sake of comparison. Except for the *Barbara* image that we used HWD-F with $l_1 = l_2 = 3$, for the other images, we used HWD-H with $l_1 = l_2 = 2$. Similar to the NLA experiment, for contourlets we used $\{l_j\}_{1 \leq j \leq 5} = \{5,4,4,3,3\}$ directional levels.

The left part of Table IV shows the PSNR values of the denoising results for different images and noise levels using hard

TIWT; PSNR = 30.97 DTCWT; PSNR = 30.91 TIHWD; PSNR = 31.18

Fig. 17. Denoising results of the *Peppers* image when $\sigma = 20$.

TABLE IV
PSNR VALUES OF THE DENOISING EXPERIMENTS LEFT PART: DIFFERENT TRANSFORMS WITH HARD THRESHOLDING. RIGHT PART: DIFFERENT DENOISING METHODS

Image	σ	Noisy Image	Wiener	WT	CT [15]	HWD	TIWT	DTCWT [23]	CuTFW [7]	TICT [17]	TIHWD	DTCWT (BS)[37]	STICT (BS)[17]	BLS-GSM [34]	TIHWD (BS)
Barbara	10	28.13	28.31	29.86	29.78	30.07	32.58	32.66	32.99	33.49	**33.70**	33.50	34.42	34.40	**34.46**
	20	22.15	26.44	25.80	26.31	26.58	28.26	28.93	29.47	29.53	**30.01**	29.78	30.59	30.60	**30.78**
	40	16.38	23.65	22.44	22.94	23.16	24.53	25.02	25.91	25.70	**26.33**	26.35	26.77	26.70	**27.15**
	60	13.30	21.75	20.99	21.04	21.21	22.82	23.00	23.73	23.57	**23.96**	24.28	24.48	24.41	**24.84**
Boats	10	28.14	30.44	30.76	30.30	30.86	33.32	33.24	32.86	33.59	**33.70**	34.02	34.35	**34.69**	34.50
	20	22.18	28.36	27.21	26.88	27.29	29.75	29.80	29.56	30.03	**30.13**	30.63	30.73	**31.14**	30.96
	40	16.42	25.09	23.83	23.55	23.82	26.32	26.20	26.29	26.49	**26.66**	27.36	27.15	**27.65**	27.48
	60	13.37	22.76	21.94	21.53	21.77	24.17	23.98	24.18	24.26	**24.42**	25.25	24.87	**25.43**	25.24
GoldHill	10	28.13	30.31	29.97	29.72	30.02	32.07	31.98	31.86	32.10	**32.36**	32.82	32.98	**33.27**	33.25
	20	22.17	28.60	26.98	26.84	27.05	29.17	29.16	29.12	29.16	**29.44**	29.97	29.93	**30.31**	30.22
	40	16.41	25.49	23.93	23.82	24.00	26.32	26.02	26.33	26.35	**26.63**	27.26	27.01	**27.49**	27.37
	60	13.34	23.09	22.09	21.88	22.08	24.40	23.94	24.40	24.57	**24.71**	25.40	25.05	**25.54**	25.44
Lena	10	28.13	32.66	32.10	31.58	32.08	34.53	34.71	34.22	**34.89**	34.73	35.30	35.44	**35.60**	35.39
	20	22.13	30.00	28.58	28.16	28.59	31.35	31.45	31.10	**31.75**	31.60	32.35	32.30	**32.63**	32.40
	40	16.35	26.10	24.97	24.64	24.92	27.83	27.67	27.71	**28.22**	28.17	29.24	28.82	**29.39**	29.15
	60	13.27	23.48	22.94	22.42	22.73	25.50	25.25	25.40	**25.82**	25.80	26.96	26.38	**27.03**	26.78
Peppers	10	28.25	32.87	31.83	31.04	31.69	33.91	33.99	33.25	**34.00**	33.95	34.27	34.43	**34.57**	34.44
	20	22.32	30.09	28.49	27.89	28.43	30.97	30.91	30.43	31.15	**31.18**	31.49	31.60	**31.92**	31.72
	40	16.59	25.79	24.47	24.09	24.46	27.06	26.79	26.83	27.26	**27.44**	28.00	27.77	**28.21**	28.14
	60	13.53	22.90	22.00	21.64	21.91	24.38	24.04	24.27	24.56	**24.71**	25.41	25.04	25.42	**25.44**

thresholding. As seen, the HWD transform yields better PSNR values than the CT. Moreover, for the *Barbara* image it achieves superior results when compared with the WT. In the case of *translation-invariant* (TI) denoising, we see that the proposed TIHWD denoising scheme almost always provides better results (improvements up to 1.80 dB) when compared with the TIWT and DTCWT schemes. Moreover, it outperforms curvelet (CuTFW) denoising scheme.

As an example of the visual results for this part of denoising, in Fig. 17, we show the TI denoising results of the *Peppers* image when $\sigma = 20$. We see that the TIHWD scheme provides less visible artifacts in the denoised image.

In the second part of denoising experiment, we took advantage of the *bivariate shrinkage* (BS) scheme with local variance estimation [37] for TIHWD, where we also used this approach for *semi-translation invariant contourlet transform* (STICT) in [17]. For TIHWD (BS), we used a window size equal to (17, 17) for estimation of local variance whereas we used a window with size (5, 5) for STICT (BS). We also compared our method to some other leading denoising approaches: DTCWT (BS) [37] and Bayes least squares using Gaussian scales mixtures (BLS-GSM) [34].

The right part of Table IV shows PSNR values resulting from the above methods. We see that for the image *Barbara*, our TIHWD (BS) denoising scheme provides better results whereas for other images it shows comparable performance (within 0.25 dB). Our results are also comparable to those reported in [13] for nonsubsampled contourlet transform using local adaptive shrinkage (NSCT-LAS).

Fig. 18 demonstrates a visual example for this part for the *Barbara* image and noise level of $\sigma = 40$. It clearly shows the superior performance of the TIHWD in retaining details along with introducing fewer (or comparable) artifacts in the result.

VI. CONCLUSION

We proposed a new family of nonredundant geometrical image transforms by employing wavelets and directional filter banks. We showed that, to avoid artifacts introduced during nonlinear approximation (and, thus, coding and denoising),

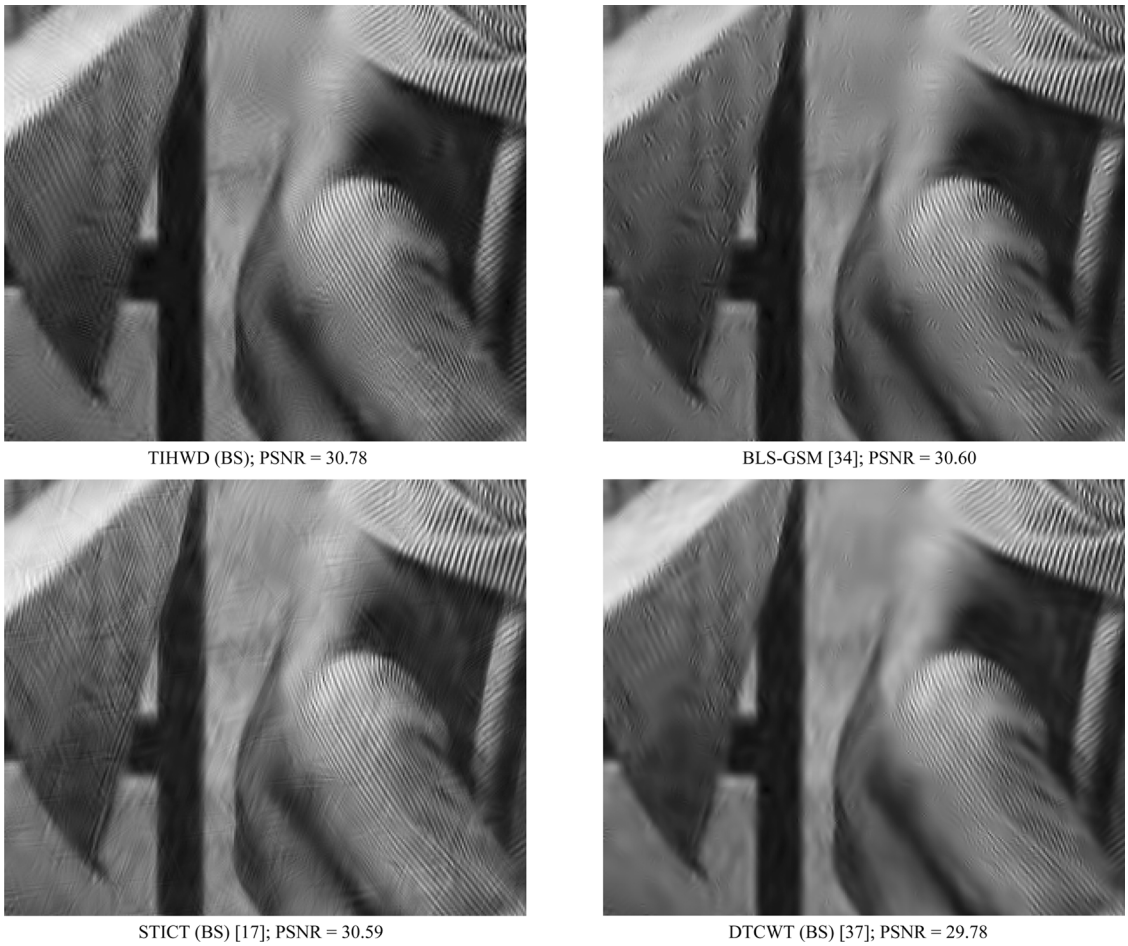

Fig. 18. Denoising results of the *Barbara* image when $\sigma = 40$.

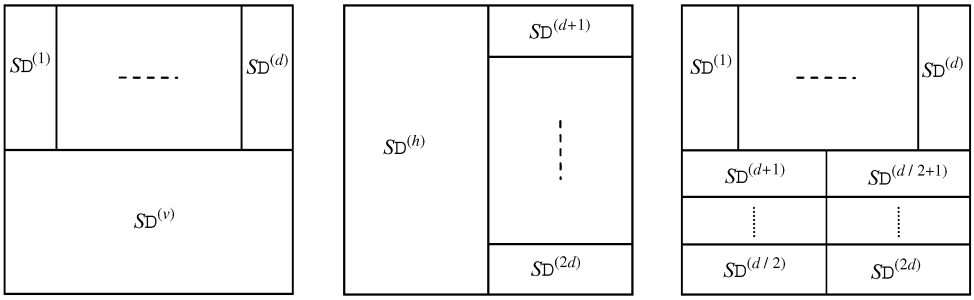

Fig. 19. Schematic diagram of the directional subbands using l levels ("S" is "H" or "V," and $d = 2^{l-1}$). *Left*: Subbands obtained by applying HDFB to a wavelet highpass channel. *Middle*: Subbands obtained by applying VDFB. *Right*: Subbands obtained by applying full-tree DFB.

we should change the wavelet basis functions in only a few finest wavelet scales. This way, we take advantage of both directional and nondirectional basis functions to efficiently represent natural images. The proposed family benefit from a number of essential characteristics. They are nonredundant and at the same time provide promising nonlinear approximation behavior for natural images especially those having a significant amount of periodic texture. Consequently, they have potential for image coding. In the experiments, we employed the proposed transform family in nonlinear approximation, image coding, and image denoising and demonstrated their efficiency in these applications.

APPENDIX I

The Rearrangement Algorithm: For each of the three types of the subbands in the levels $1 \leq j \leq J_m$, we utilize its individual algorithm described as follows (see Fig. 19).

1) For subbands to which a HDFB is applied: Suppose we decompose a wavelet subband of size $N_s \times N_s$, into $d = 2^{l-1}$ horizontal directional subbands $S\mathbb{D}^{(i)}$ ($1 \leq i \leq d$, "S" is either "H" or "V"), each having a size of $\tilde{M} \times \tilde{m}$, where $\tilde{M} = N_s/2$, and $\tilde{m} = N_s/d$. Now we combine these directional subbands columnwise to form $S\mathbb{D}^{(H)}$ as: $S\mathbb{D}^{(H)} = [c_1^{h_1} \ \ldots \ c_1^{h_d} \ \ldots \ c_{\tilde{m}}^{h_1} \ \ldots \ c_{\tilde{m}}^{h_d}]$, where c_i^x denotes the column i of subband $S\mathbb{D}^{(x)}$. To form a subband

almost similar to a wavelet subband, we combine the resulting matrix with $S\mathrm{D}^{(v)}$ row-wise to obtain $\tilde{S}_{\mathrm{HDFB}} = [r_1^H r_1^v \ \cdots \ r_{\tilde{M}}^H r_{\tilde{M}}^v]^T$, where r_i^x denotes the row i of subband $S\mathrm{D}^{(x)}$ and $(\cdot)^T$ denotes the transpose operation.

2) For subbands to which a VDFB is applied: Here, we use the *dual* procedure of the one we used to rearrange the HDFB subbands. That is, we first combine the vertical directional subbands row-wise, and then we interlace the resulting matrix with $S\mathrm{D}^{(h)}$, columnwise to obtain $\tilde{S}_{\mathrm{VDFB}}$.

3) For subbands to which a full DFB is applied: In this case, we first combine the horizontal subbands to obtain $S\mathrm{D}^{(H)} = [c_1^{h_1} \ \cdots \ c_1^{h_d} \ \cdots \ c_{\tilde{m}}^{h_1} \ \cdots \ c_{\tilde{m}}^{h_d}]$. Now we divide the vertical subbands into two parts and combine each part row-wise separately as $S\mathrm{D}^{(V_1)} = [r_1^{v_1} \ \cdots \ r_1^{v_\delta} \ \cdots \ r_{\tilde{m}}^{v_1} \ \cdots \ r_{\tilde{m}}^{v_\delta}]^T$, and $S\mathrm{D}^{(V_2)} = [r_1^{v_{\delta+1}} \ \cdots \ r_1^{v_d} \ \cdots \ r_{\tilde{m}}^{v_{\delta+1}} \ \cdots \ r_{\tilde{m}}^{v_d}]^T$, where $\delta = d/2$. Interlacing the resulting matrices columnwise, we obtain $S\mathrm{D}^{(\hat{V})}$, which is the same size as $S\mathrm{D}^{(H)}$: $S\mathrm{D}^{(\hat{V})} = [c_1^{V_1} c_1^{V_2} \ \cdots \ c_{\tilde{M}}^{V_1} c_{\tilde{M}}^{V_2}]$. Finally, we interlace $S\mathrm{D}^{(H)}$ and $S\mathrm{D}^{(\hat{V})}$ row-wise and obtain $\tilde{S}_{\mathrm{DFB}} = [r_1^H r_1^{\hat{V}} \ \cdots \ r_{\tilde{M}}^H r_{\tilde{M}}^{\hat{V}}]^T$.

REFERENCES

[1] R. Ansari, C. W. Kim, and M. Dedovic, "Structure and design of two-channel filter banks derive from a triplet of halfband filters," *IEEE Trans. Circuits Syst. II, Exp. Briefs*, vol. 46, no. 12, pp. 1487–1496, Dec. 1999.

[2] R. H. Bamberger, "New results on two and three dimensional directional filter banks," in *Proc. Asilomar Conf. Signals, Systems, and Computers*, 1993, vol. 2, pp. 1286–1290.

[3] ——, "New subband decompositions and coders for image and video compression," in *Proc. of IEEE Int. Conf. Acoustics, Speech, Signal Processing*, Mar. 1992, vol. 3, pp. 217–220.

[4] R. H. Bamberger and M. J. T. Smith, "A filter bank for the directional decomposition of images: Theory and design," *IEEE Trans. Signal Process.*, vol. 40, no. 4, pp. 882–893, Apr. 1992.

[5] P. Brodatz, *Textures, a Photographic Album for Artists and Designers* [Online]. Available: http://www.ux.his.no/~tranden/brodatz.html

[6] P. J. Burt and E. H. Adelson, "The Laplacian pyramid as a compact image code," *IEEE Trans. Commun.*, vol. 31, no. 4, pp. 532–540, Apr. 1983.

[7] E. J. Candes, L. Demanet, D. Donoho, and L. Ying, "Fast discrete curvelet transform," *Multiscale Model. Simul.* vol. 5, no. 3, pp. 861–899, Sep. 2006 [Online]. Available: http://www.curvelet.org/software.html

[8] E. J. Candes and D. L. Donoho, "Curvelets—A surprisingly effective nonadaptive representation for objects with edges," in *Curve and Surface Fitting*. Nashville, TN: Vanderbuilt Univ. Press, 1999.

[9] ——, "New tight frames of curvelets and optimal representations of objects with piecewise C^2 singularities," *Commun. Pure Appl. Math.*, vol. 57, pp. 219–266, Feb. 2004.

[10] E. Chang and A. Zakhor, "Subband video coding based on velocity filters," in *Proc. IEEE Int. Conf. Circuits Syst.*, May 1992, vol. 5, pp. 2288–2291.

[11] A. Cohen, I. Daubechies, O. Guleryuz, and M. Orchard, "On the importance of combining wavelet-based non-linear approximation with coding strategies," *IEEE Trans. Inf. Theory*, vol. 48, no. 7, pp. 1895–1921, Jul. 2002.

[12] R. R. Coifman and D. L. Donoho, "Translation invariant de-noising," in *Wavelets and Statistics*. New York: Springer-Verlag, 1995, vol. 103, pp. 125–150.

[13] A. L. da Cunha, J. Zhou, and M. N. Do, "The nonsubsampled contourlet transform: Theory, design, and applications," *IEEE Trans. Image Process.*, vol. 15, no. 10, pp. 3089–3101, Oct. 2006.

[14] M. N. Do, "Directional multiresolution image representations," Ph.D. dissertation, EPFL, Lausanne, Switzerland, Dec. 2001.

[15] M. N. Do and M. Vetterli, "The contourlet transform: An efficient directional multiresolution image representation," *IEEE Trans. Image Process.* vol. 14, no. 12, pp. 2091–2106, Dec. 2005 [Online]. Available: http://www.ifp.uiuc.edu/~minhdo/software/

[16] D. L. Donoho and I. M. Johnstone, "Ideal spatial adaptation by wavelet shrinkage," *Biometrika*, vol. 81, no. 3, pp. 425–455, 1994.

[17] R. Eslami and H. Radha, "Translation-invariant contourlet transform and its application to image denoising," *IEEE Trans. Image Process.*, vol. 15, no. 11, pp. 3362–3374, Nov. 2006.

[18] ——, "New image transforms using hybrid wavelets and directional filter banks: Analysis and design," in *Proc. IEEE Int. Conf. Image Processing*, Genova, Italy, Sep. 2005, vol. 1, pp. 733–736.

[19] R. Eslami and H. Radha, "Regular hybrid wavelets and directional filter banks: Extensions and applications," presented at the IEEE Int. Conf. Image Processing, Atlanta, GA, Oct. 2006.

[20] ——, "Wavelet-based contourlet coding using an SPIHT-like algorithm," in *Proc. Conf. Information Sciences, Systems*, Princeton, NJ, Mar. 2004, pp. 784–788.

[21] ——, "Wavelet-based contourlet transform and its application to image coding," in *Proc. IEEE Int. Conf. Image Processing*, Singapore, Oct. 2004, vol. 5, pp. 3189–3192.

[22] F. C. A. Fernandes, R. L. C. van Spaendonck, and C. S. Burrus, "Multidimensional, mapping-based complex wavelet transforms," *IEEE Trans. Image Process.*, vol. 14, no. 1, pp. 110–124, Jan. 2005.

[23] N. G. Kingsbury, "Complex wavelets for shift invariant analysis and filtering of signals," *Appl. Comput. Harmon. Anal.* vol. 10, no. 3, pp. 234–253, May 2002 [Online]. Available: http://taco.poly.edu/WaveletSoftware/dt2D.html

[24] J. Kovacevic and M. Vetterli, "Nonseparable multidimensional perfect reconstruction filter banks and wavelet bases for $\mathbb{R}$," *IEEE Trans. Inf. Theory*, vol. 38, pp. 533–555, Mar. 1992.

[25] ——, "Nonseparable two- and three-dimensional wavelets," *IEEE Trans. Signal Process.*, vol. 43, no. 5, pp. 1269–1273, May 1995.

[26] E. LePennec and S. Mallat, "Sparse geometric image representation with bandelets," *IEEE Trans. Image Process.*, vol. 14, no. 4, pp. 423–438, Apr. 2005.

[27] Y. Lu and M. N. Do, "CRISP-contourlets: A critically sampled directional multiresolution image representation," presented at the Proc. SPIE Conf. Wavelet Applications in Signal and Image Processing X, San Diego, CA, Aug. 2003.

[28] S. Mallat, *A Wavelet Tour of Signal Processing*, 2nd ed. New York: Academic, 1998.

[29] T. T. Nguyen and S. Oraintara, "Multiresolution direction filterbanks: Theory, design, and applications," *IEEE Trans. Signal Process.*, vol. 53, no. 10, pp. 3895–3905, Oct. 2005.

[30] A. V. Oppenheim, R. W. Schafer, and J. R. Buck, *Discrete-Time Signal Processing*, 2nd ed. Englewood Cliffs, NJ: Prentice-Hall, 1999.

[31] S. Park, M. J. T. Smith, and R. M. Mersereau, "Improved structures of maximally decimated directional filter Banks for spatial image analysis," *IEEE Trans. Image Process.*, vol. 13, no. 11, pp. 1424–1431, Nov. 2004.

[32] S. M. Phoong, C. W. Kim, P. P. Vaidyanathan, and R. Ansari, "A new class of two-channel biorthogonal filter banks and wavelet bases," *IEEE Trans. Signal Process.*, vol. 43, no. 3, pp. 649–665, Mar. 1995.

[33] D. D.-Y. Po and M. N. Do, "Directional multiscale modeling of images using the contourlet transform," *IEEE Trans. Image Process.*, vol. 15, no. 6, pp. 1610–1620, Jun. 2006.

[34] J. Portilla, V. Strela, M. J. Wainwright, and E. P. Simoncelli, "Image denoising using scale mixtures of Gaussians in the wavelet domain," *IEEE Trans. Image Process.* vol. 12, no. 11, pp. 1338–1351, Nov. 2003 [Online]. Available: http://decsai.ugr.es/~javier/denoise/index.html

[35] A. Said and W. A. Pearlman, "A new fast and efficient image codec based on set partitioning in hierarchical trees," *IEEE Trans. Circuits Syst. Video Technol.*, vol. 6, no. 3, pp. 243–250, Jun. 1996.

[36] L. Sendur and I. W. Selesnick, "Bivariate shrinkage functions for wavelet-based denoising exploiting interscale dependency," *IEEE Trans. Signal Process.*, vol. 50, no. 11, pp. 2744–2756, Nov. 2002.

[37] ——, "Bivariate shrinkage with local variance estimation," *IEEE Signal Process. Lett.*, vol. 9, no. 12, pp. 438–441, Dec. 2002.

[38] P. P. Vaidyanathan, *Multirate Systems and Filter Banks*. Englewood Cliffs, NJ: Prentice-Hall, 1993.

[39] V. Velisavljevic, B. Beferull-Lozano, M. Vetterli, and P. L. Dragotti, "Directionlets: Anisotropic multidirectional representation with separable filtering," *IEEE Trans. Image Process.*, vol. 15, no. 7, pp. 1916–1933, Jul. 2001.

[40] M. Vetterli, "Wavelets, approximation and compression," *IEEE Signal Process. Mag.*, vol. 18, no. 5, pp. 59–73, Sep. 2001.

[41] M. Vetterli and J. Kovacevic, *Wavelets and Subband Coding*. Englewood Cliffs, NJ: Prentice-Hall, 1995.
[42] M. Wakin, J. K. Romberg, H. Choi, and R. G. Baraniuk, "Wavelet-domain approximation and compression of piecewise smooth images," *IEEE Trans. Image Process.*, vol. 15, no. 5, pp. 1071–1087, May 2006.
[43] Z. Xiong, K. Ramchandran, and M. Vetterli, "Space-frequency quantization for wavelet image coding," *IEEE Trans. Image Process.*, vol. 6, no. 5, pp. 677–693, May 1997.

Ramin Eslami (S'02–M'06) received the B.S. degree in electrical engineering from Iran University of Science and Technology, Tehran, Iran, in 1994, the M.S. degree in biomedical engineering from Sharif University of Technology, Tehran, in 1997, and the Ph.D. degree in electrical engineering from Michigan State University (MSU), East Lansing, in 2006.

Currently, he is a Postdoctoral Fellow in the Department of Electrical and Computer Engineering, McMaster University, Hamilton, ON, Canada. From 2002 to 2006, he was a Research Assistant in the Department of Electrical and Computer Engineering, MSU. He was an Instructor in the Electrical Engineering Department, Aeronautical University of Shahid Sattari, Tehran, from 1998 to 2000. His research interests include image and multidimensional signal processing, wavelets and filter banks, coding, denoising, and watermarking.

Hayder Radha (M'92–SM'01) received the B.S. degree (with honors) from Michigan State University (MSU), East Lansing, in 1984, the M.S. degree from Purdue University, West Lafayette, IN, in 1986, and the Ph.M. and Ph.D. degrees from Columbia University, New York, in 1991 and 1993, respectively, all in electrical engineering.

He is a Professor of electrical and computer engineering at MSU. He joined MSU in 2000 as an Associate Professor in the Department of Electrical and Computer Engineering. Between 1996 and 2000, he was with Philips Research, where he worked as a Principal Member of Research Staff and then as a Consulting Scientist in the Video Communications Research Department. At Philips Research, he initiated the Internet Video Project and led a team of researchers working on scalable video coding, networking, and streaming algorithms. He became a Philips Research Fellow in 2000. Prior to joining Philips Research, he was with Bell Labs from 1986 and 1996, where he worked in the areas of digital communications, signal/image processing, and broadband multimedia. He served as Co-Chair and Editor of the ATM and LAN Video Coding Experts Group of the ITU-T from 1994 to 1996. His research interests include coding and communications, multimedia networking, stochastic modeling, and image and video processing and compression, and he has authored more than 100 peer-reviewed papers and holds 24 U.S. patents in these areas.

Dr. Radha is a recipient of the Bell Labs Distinguished Member of Technical Staff Award, the AT&T Bell Labs Ambassador Award, AT&T Circle of Excellence Award, the Withrow Distinguished Scholar Award for outstanding contributions to engineering, and the Microsoft Research Content and Curriculum Award.